

Towards friction and adhesion from high modulus microfiber arrays

B. SCHUBERT^{1,*}, C. MAJIDI¹, R. E. GROFF², S. BAEK¹, B. BUSH³,
R. MABOUDIAN³ and R. S. FEARING¹

¹ *Department of Electrical Engineering & Computer Sciences, University of California, Berkeley, California 94720, USA*

² *Department of Electrical & Computer Engineering, Clemson University, Clemson, South Carolina 29634, USA*

³ *Department of Chemical Engineering, University of California, Berkeley, California 94720, USA*

Received in final form 8 August 2007

Abstract—Unlike traditional pressure sensitive adhesives, the natural setal arrays of gecko lizards achieve dry adhesion with stiff, keratinous material. This remarkable property has inspired a new class of adhesive and high friction microstructures composed of stiff materials that, like natural setae, have an elastic modulus greater than 1 GPa. In contrast to softer materials, such as rubber and low molecular weight acrylates, stiff materials have the advantage of wear and creep resistance and represent a wide range of polymers, metals, and ceramics that include materials that are also temperature resistant and biocompatible. This work presents progress in the design and fabrication of synthetic gecko adhesives with particular attention to the principles of contact mechanics and elasticity that are essential in formulating accurate design criteria.

Keywords: Bio-inspired adhesion; fibrillar adhesives; microfabrication; elastic rod theory.

1. INTRODUCTION

Since the discovery that the gecko's elaborate adhesive structures rely significantly on van der Waals forces [1, 2], a number of researchers have sought to mimic the lizard's clinging capabilities. Synthetic gecko-adhesives have primarily taken the form of dense arrays of fibers, as this is the most basic and easily reproduced facet of the gecko's hierarchical structure. However, to date only a few synthetic materials have started to show some aspects of gecko-like behavior [3–9].

One possible path to success is to make slender, high aspect ratio structures with correspondingly high density. Such structures are generally prone to self-adhesion

*To whom correspondence should be addressed. E-mail: bschuber@eecs.berkeley.edu

[10, 11] unless they have a high stiffness and adequate spacing. For instance, multi-walled carbon nanotubes (MWCNTs) avoid severe clumping because of their high modulus of elasticity E . They are also able to overcome their inherent stiffness to produce adhesion [4] through bending into side contact [12]. However, whereas the gecko's fibers last months between molting cycles [13], the nanotubes start to deteriorate after only a few uses due to entanglement and fibers breaking off from the backing material.

Some success has been obtained with the arrays of vertically aligned, low-aspect ratio pillars that are either fabricated from soft polymer ($E \sim 1$ MPa) [5, 7, 14] or supported by a pressure sensitive adhesive (PSA) [15]. These structures represent steps towards fibrillar adhesion, but the soft nature of the fibers will limit any other similarities to the gecko, such as resistance to wear and particulate contamination [13].

In terms of modulus, the gecko fits into the middle of the two extremes between carbon nanotubes and soft polymers. It provides a principal example of how geometry can be used to turn a stiff material ($E \sim 1$ GPa) into something as compliant as a pressure sensitive adhesive ($E_{\text{eff}} \sim 80$ kPa) [16] while maintaining desirable properties of a stiff bulk material.

Fiber arrays composed of stiff polymers, stiffness on the order of that of the gecko, are showing promising results in terms of high friction [6] and modest shear adhesion. Figure 1 shows a polypropylene ($E = 1$ GPa) array of $0.6 \mu\text{m}$ diameter, $20 \mu\text{m}$ long fibers able to support a coin through friction, and a 100 g weight in pure shear. In addition, it is commonly accepted that a high modulus correlates to a high melting temperature [17], low coefficient of expansion [18] and high resistance to wear [19].

To develop more effective fiber arrays, it is necessary to first model and understand the behavior of fibrillar structures. In this paper, classical beam theory, including Euler–Bernoulli and column buckling, are used to get a first-order approximation of the problem, and then higher level models, like elastica, are employed for more accurate predictions.

To test the models, we present methods for fabricating stiff arrays from polymers such as polypropylene (PP) and polyimide (PI) ($E = 3$ GPa) as well as from nickel ($E = 200$ GPa). These fiber arrays show some undesirable properties like clumping, length variation and substrate curvature, but we have developed theories to explain these phenomena and methods to mitigate their effects. We also developed an apparatus for measuring tangential and normal forces at different size scales. For macro-scale tests, a classical pulley apparatus is sufficient, but for the smaller scale we have assembled a two-axis force sensor with a spherical probe. This provides insight into the specific regions of a sample.

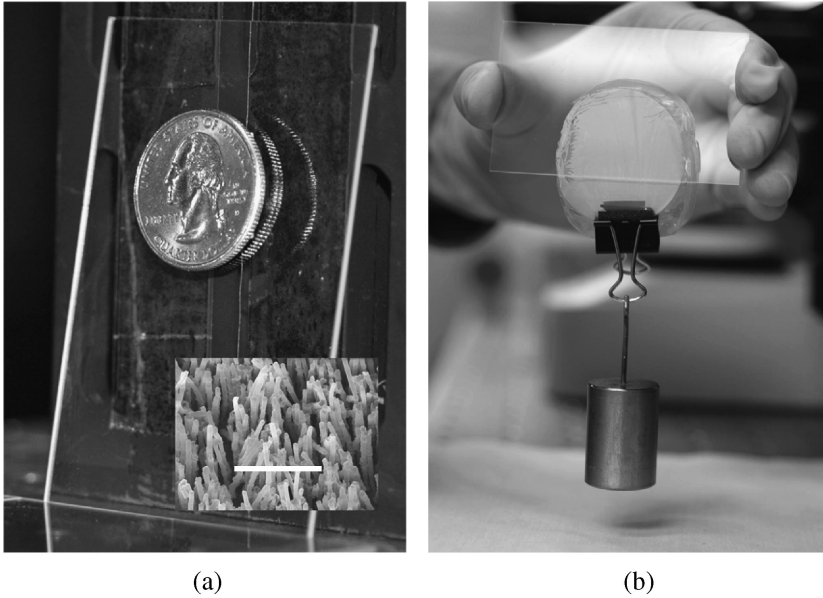


Figure 1. Array of 0.6 μm diameter, 20 μm long polypropylene fibers supporting (a) an American quarter at a slight angle and (b) a 100 g weight in pure shear. The inset picture in (a) is an SEM micrograph of the fiber array. Scale bar is 10 μm .

2. MATHEMATICAL MODELS OF NATURAL AND SYNTHETIC SETAE

Design criteria for fiber array adhesives are derived from mathematical models that treat the synthetic fibers as planar elastic rods. The deformed configuration of the rod is parameterized in two dimensions by the angular deflection $\theta = \theta(\xi)$ with respect to a fixed, rectilinear axis. The coordinate ξ denotes the arc length between the support and a point on the rod. At the tip, $\xi = L$, where L is the fiber length. For the structures of interest, the fiber is cylindrical and thus has a bending stiffness EI , where E is the elastic modulus, $I = \pi R^4/4$ is the area moment of inertia, and R is the fiber radius.

The primary aim of the elastic rod model is to establish a relationship between tip displacement and the magnitude and direction of externally applied load. Typically, fibers will be loaded at the tip by a combination of friction and adhesion or compressive forces. These forces generate an internal moment $M = M(\xi)$, which is related to $\theta = \theta(\xi)$ through the constitutive relationship

$$M = EI \frac{d\theta}{d\xi} \quad \Rightarrow \quad \frac{dM}{d\xi} = EI \frac{d^2\theta}{d\xi^2}. \quad (1)$$

In general, an elementary solution to (1) is only possible by linearizing (1) about the undeformed configuration. This yields models for Euler–Bernoulli beam bending and ideal column buckling. In cases for which linearization is not admissible, the complete solution is obtained with elastica theory.

2.1. Euler–Bernoulli beam model

For small deflections ($|\theta| < \pi/12$) induced by a shear force S on the tip, it is convenient to employ the approximations $\sin \theta \approx \theta$ and $\cos \theta \approx 1$. These assumptions yield the Euler–Bernoulli beam equation:

$$\frac{d^2\theta}{d\xi^2} - \frac{1}{EI}\{S(L - \xi)\} = 0. \tag{2}$$

2.1.1. Compliance of angled microfibers. Euler–Bernoulli beam theory is used to estimate the bending compliance of a fiber that has a natural deflection ϕ from the normal to the supporting plane, denoted by \mathbf{n} (see Fig. 2a). Loading the fiber tip by a force F in the $-\mathbf{n}$ direction results in a shear force $S = F \sin \phi$. From (2) it follows that the tip is displaced by an amount u in the $-\mathbf{n}$ direction and that F/u is equal to the constant

$$k = \frac{3EI}{L^3 \sin^2 \phi}. \tag{3}$$

Assuming that the tips are rounded and have a radius of curvature R_t equal to the fiber radius, i.e. $R_t = R$, it follows from the Johnson–Kendall–Roberts theory that the maximum tensile load on each fiber is $F_0 = 1.5\pi RW_{ad}$, where W_{ad} is the interfacial work of adhesion [20]. This corresponds to a tip displacement $u_0 = F_0/k$.

The mechanical behavior of an array of microfibers is characterized by an effective elastic modulus E_{eff} , which relates stresses and strains. For a fiber density D , Ref. [16] shows that

$$E_{eff} = kDL \cos \phi = \frac{3EID \cos \phi}{L^2 \sin^2 \phi}. \tag{4}$$

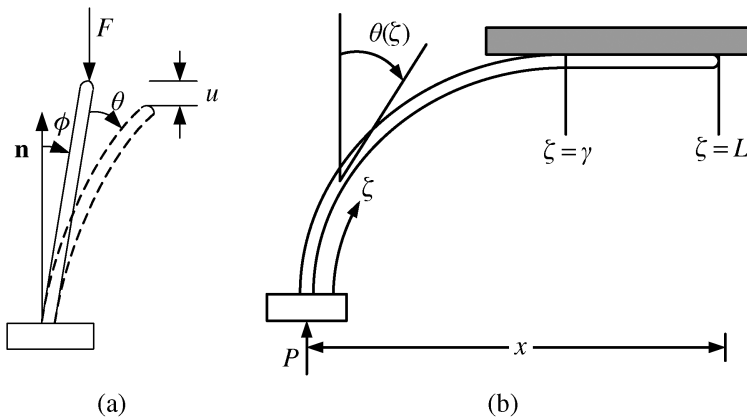


Figure 2. The two principal beam bending models used are (a) the Euler–Bernoulli beam and (b) the elastica models.

For tokay setae, $D = 1.44 \times 10^{10} \text{ m}^{-2}$, $E = 1.5 \text{ GPa}$, $L = 100 \text{ }\mu\text{m}$, $R = 2 \text{ }\mu\text{m}$, and $\phi = 45^\circ$. Hence, $E_{\text{eff}} = 115 \text{ kPa}$, which is well below Dahlquist's limit for tack ($E < 300 \text{ kPa}$ at 1 Hz) [21] and implies that the setal array has the compliance necessary to exhibit pressure sensitive adhesion. Moreover, this result is consistent with experimental measurements on natural setal arrays [16].

2.2. Ideal column buckling model

A column buckling model for gecko adhesion was first proposed by Jagota and Bennison [22], but normal adhesion forces will be small without side contact. Column buckling can be used to provide a low effective modulus. For vertical fibers (i.e. $\phi = 0$), (3) predicts that $u = 0$ for all $F > 0$. This result, however, is an artifact of the linearization $\cos \theta = 1$. According to the exact solution to (1), displacement along $-\mathbf{n}$ occurs when F exceeds a critical force F_{cr} . In general,

$$F_{\text{cr}} = \frac{\pi^2 EI}{(KL)^2}, \quad (5)$$

where K is the effective length factor and depends on the buckling mode. According to the ideal column buckling model,

$$u = 0 \iff F < F_{\text{cr}} \quad \text{and} \quad u > 0 \iff F = F_{\text{cr}}. \quad (6)$$

2.2.1. Spherical indentation of microfibers. Figure 3a shows a fiber array pushed upward into a spherical probe until the probe reaches some maximum depth of penetration. Then the sample is retracted along the same path. This situation is

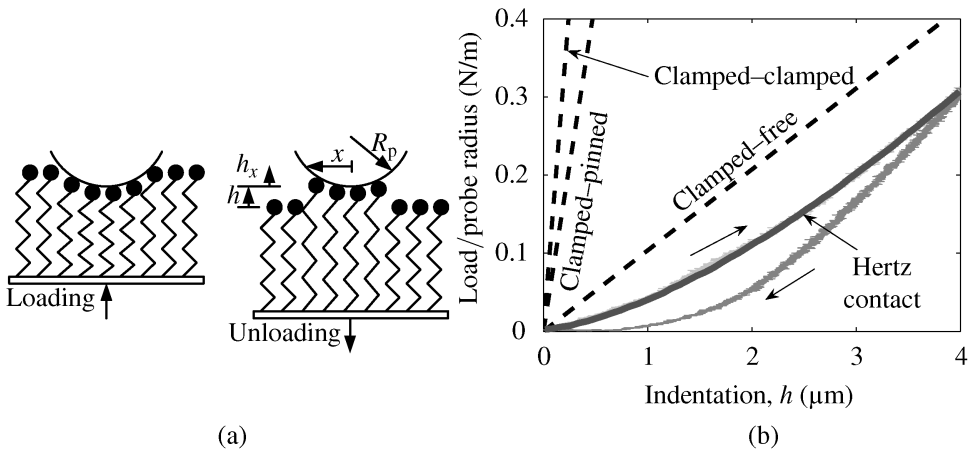


Figure 3. (a) Illustration of loading and unloading cycle for a spherical probe, and (b) mechanical response of $R = 0.3 \text{ }\mu\text{m}$ non-adhesive fiber array indented by a spherical probe (radius = 5.17 cm); (---) theoretical predictions based on ideal column buckling for clamped-free ($K = 2$), clamped-pinned (0.7), and clamped-clamped (0.5) buckling; (—) shows a fit using the Hertz contact theory with $E_{\text{eff}} = 6.5 \text{ MPa}$; arrows indicate loading direction.

modeled with fibers of area density D , and acting as vertical springs with spring constant k , as given in (3). The maximum distance a fiber can stretch before detaching is then $u_0 = F_0/k$.

The height of the lowest point on the probe from the neutral plane of the fiber tips is given by h , which is positive above the plane. Because the radius of the probe, R_p , is large compared to the contact area, we can use a quadratic approximation to find the distance from the probe to the fiber tip plane, $h + h_x = h + x^2/2R_p$. The force applied to the fibers by the probe is

$$F_s = \int_0^{r_c} 2\pi x D(-k)(h + x^2/2R_p) dx = -2\pi Dk \left(\frac{hr_c^2}{2} + \frac{r_c^4}{8R_p} \right), \quad (7)$$

where r_c is the contact radius, and positive values of F_s indicate compression. This same expression for force applies both during loading and unloading. The hysteresis, illustrated in Fig. 3b, arises due to contact hysteresis. During loading, the contact radius is $r_c = \sqrt{-2R_p h}$, while during unloading the contact radius is $r_c = \sqrt{2R_p(u_0 - h)}$. The maximum adhesion force during unloading is given by $F_{\text{unload}} = -\pi R_p D k u_0^2$.

For vertical columns, the force measured by the probe is related to the critical buckling load as $F_s = 2\pi R_p D F_{\text{cr}} h$. A typical plot of F_s/R_p versus h is presented in Fig. 3b for a probe of radius 5.17 cm and an array of polypropylene microfibers of length $L = 20 \mu\text{m}$, radius $R = 0.3 \mu\text{m}$, modulus $E = 1 \text{ GPa}$, and density $D = 42 \times 10^6 \text{ cm}^{-2}$. This measurement is obtained using the optical force sensing apparatus described in Appendix A.2. Among the various column buckling modes, the clamped-free mode most closely matches the measured response, so setting $K = 2$ in (5) gives a critical buckling load of $F_{\text{cr}} = 39 \text{ nN}$. However, at lower indentation the clamped-free mode overestimates the stiffness. This may be a result of fiber length variation, which causes the array to be more sparse at heights close to $20 \mu\text{m}$. Regardless, the clamped-free buckling model is adopted as it produces the best estimate for the mechanical response.

If one wants an exact fit to the loading curve, one can use the Hertz contact theory [23] and adjust the effective elastic modulus, E_{eff} , to account for issues that the buckling model neglects, such as fiber length variation. The Hertz model for a rigid sphere indenting a planar, elastic surface with normal force F gives:

$$F = \frac{4E_{\text{eff}}}{3(1-\nu^2)} \sqrt{R_p h^3}. \quad (8)$$

Poisson's ratio, ν , is zero for fiber arrays because compressive strain is not transmitted laterally. Figure 3b shows a fit of (8) to the loading curve. With probe radius, R_p , set to 5.17 cm we find that $E_{\text{eff}} = 6.5 \text{ MPa}$ generates a very close fit of the curve. This shows that the fibers are nearly 100 times more compliant than bulk polypropylene which has $E = 1 \text{ GPa}$. However, they are not compliant enough to be considered tacky by Dahlquist's criterion, so this is one possible reason why they do not exhibit pull-off (normal) adhesion.

2.2.2. Friction coefficient of microfiber array. Vertically aligned microfiber arrays under compression can achieve compliance through buckling, allowing them to exhibit a high resistance to frictional drag. This property follows from the adhesion theory of friction, which states that the maximum shear force S for a prescribed normal load F is proportional to the real area of contact A_r . For ideal column buckling, (6) implies that the number of fibers in contact is approximately $N = F/F_{cr}$ and that the load on each contacting fiber is F_{cr} . Assuming rounded tips of radius R_t , the contact area for each fiber is calculated from the JKR theory [20].

By Coulomb's law, the shear strength of each fiber tip is $S_f = \mu F_{cr} + \tau A_f$, where τ is the interfacial shear strength per unit area of real contact, and the equivalent friction relation, V , is

$$V = \hat{\mu}F, \quad \hat{\mu} = \mu + \tau A_f/F_{cr}. \quad (9)$$

Interestingly, (9) resembles Amontons' law with the constant $\hat{\mu}$ as an effective coefficient of friction. As shown in Fig. 4, (9) is consistent with measurements of the coefficient of friction obtained for 0.3, 0.6 and 2.5 μm radius fibers under loads as high as 10 kPa. It is assumed that $R_t = 3R$, since this gives the closest theoretical fits for the geometries and loads of interest.

2.3. Elastica model

For axially loaded fibers undergoing large deflection (see Fig. 2b), the ideal column buckling model must be replaced with the complete nonlinear solution to the constitutive law (1). This solution involves the computation of elliptic functions

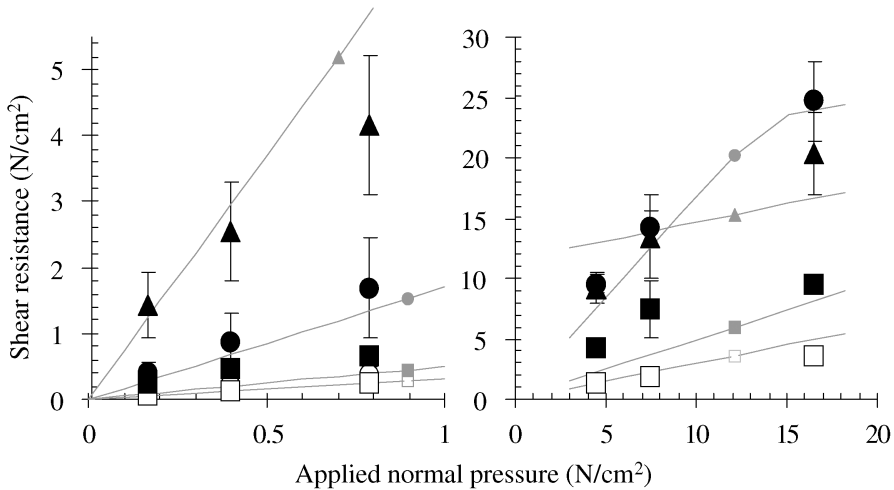


Figure 4. Plot of shear resistance *versus* applied normal pressure for polypropylene fiber arrays and controls; (▲) radius $R = 0.3 \mu\text{m}$, (●) $R = 0.6 \mu\text{m}$, (■) $R = 2.5 \mu\text{m}$, (○) unprocessed control, (□) processed control; (left) loading area = 1.27 cm^2 , sample size = 15; (right) loading area = 0.033 cm^2 , sample size = 5; error bars represent one standard deviation in the data; solid lines represent theoretical predictions for $R_t = 3R$. From [6].

and is known as the elastica. Elastica theory is essential for modeling adhesion through side contact.

2.3.1. *Side contact model.* The tensile compliance of fibers in an array of vertically aligned carbon nanotubes (VACNTs) is explained with the side contact model [12]. According to this theory, a fiber contacts an opposing surface by bending over and adhering along its side [12, 24]. For sufficiently slender fibers, the surface adhesion exceeds the elastic bending forces and allows stable side contact even under tension. According to elastica theory, adhesion through side contact is only possible when the fiber length is greater than the critical value, i.e.,

$$L_{cr} = \frac{\pi}{2} \sqrt{\frac{EI}{2\omega}}, \tag{10}$$

where ω is the energy of adhesion per unit length.

The force necessary to detach a fiber engaged in side contact varies depending on the translational constraints on the backing (see Fig. 5a) [12]. In the case of a laterally unconstrained backing, the peel strength approaches the energy of adhesion, ω , for $L \gg L_{cr}$. Interestingly, the peel strength is approximately three times greater with a laterally constrained backing. The difference between the two cases is analogous to peeling a piece of sticky tape from its end (laterally

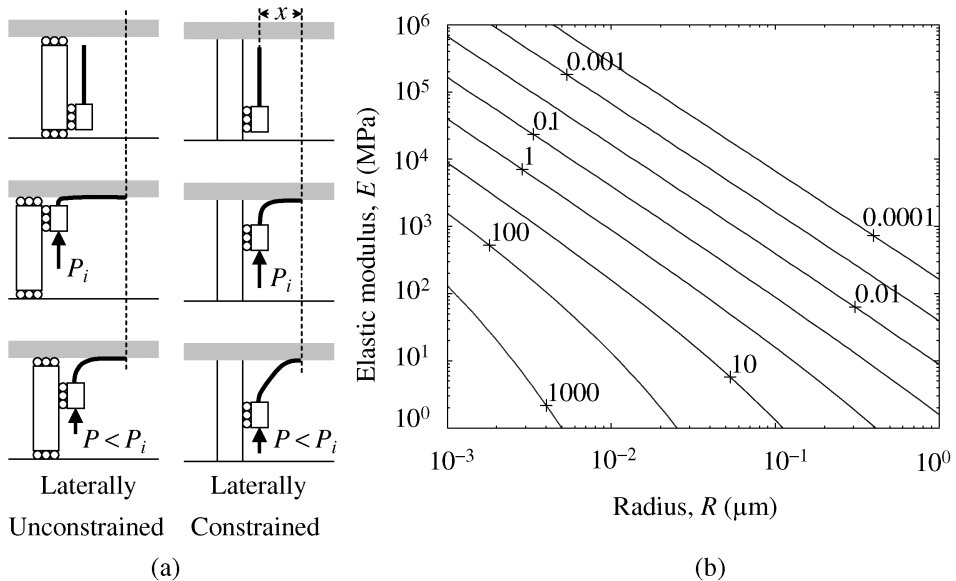


Figure 5. (a) Shows how a fiber behaves during loading for laterally-constrained and laterally-unconstrained backing. (b) Plot showing lines of constant pull-off strength, σ , in N/cm^2 for arrays of non-clumping fibers engaged in side contact, depending on elastic modulus, E , and fiber radius, R ; fibers have length L_{cr} and density D_{cr} ; $W_{ad} = 30 \text{ mJ}/\text{m}^2$ and $\nu = 1/3$.

unconstrained) *versus* its center (laterally constrained). When peeled from its center, the peel angle is much smaller, resulting in a much larger peel resistance.

Consider an array of VACNTs of length $L = 40 \mu\text{m}$, outer radius $R = 12.5 \text{ nm}$, elastic modulus $E = 200 \text{ GPa}$, and density $D = 10^{14} \text{ m}^{-2}$ [25]. Assuming a Poisson's ratio of $\nu = 0.3$ and noting that $W_{\text{ad}} = 330 \text{ mJ/m}^2$ [26], it follows from (14) that $\omega = 0.83 \text{ nN}$. The peel strength is approximated as ω and 3ω for the laterally unconstrained and constrained cases, respectively. Hence, $0.83 \text{ nN} \leq P \leq 2.5 \text{ nN}$, where P is the pull-off strength for a single fiber, and the total pull-off strength of the array, $\sigma = DP$, is in the range of $8.3\text{--}25 \text{ N/cm}^2$. Ref. [4] reports an experimental pull-off strength of 10 N/cm^2 , well within the theoretical range.

In general, adhesion through side contact is only possible when L is at least on the order of L_{cr} . For such structures, the pull-off strength is on the order of $\sigma = D\omega$, where the density D is limited by

$$D_{\text{cr}} = \frac{1}{(2R + \Delta_{\text{cr}})^2}, \quad (11)$$

where the critical spacing Δ_{cr} is presented in Section 4.1 for various clumping models. Contours of constant σ as a function of R and E are presented in Fig. 5b. Because of their low density, these structures exhibit less adhesion than the MWCNT arrays studied in [4]. However, they will not clump over repeated loadings and are thus reusable.

3. FABRICATION METHODS

3.1. Casting

Fiber casting consists of filling a mold with a given material. For example, the mold used is a $20 \mu\text{m}$ thick polycarbonate filter (ISOPORE, Millipore Inc., Billerica, MA, USA) generated by nuclear track etching to have a specific pore diameter across the filter. The diameters range from 5.0 to $0.1 \mu\text{m}$. Fig. 6a and b show that the filter can either be filled with a thermoplastic (e.g. polypropylene (PP)), or a thermoset (e.g. polyimide (PI)). Polypropylene films ranging in thicknesses from 25.4 to $4.0 \mu\text{m}$ (Premier Lab Supply Inc., Port St. Lucie, FL, USA) are pressure driven into the filter for $20\text{--}30$ minutes at 200°C in vacuum. Then, the filter is dissolved in methylene chloride. For polyimide (PI-2611, HD Microsystems Inc., Wilmington, DE, USA), the filter is filled through capillary action, and then the polyimide is cured in the filter. After curing, overfill is removed by light sanding, and the filter is etched away.

Alternatively, alumina membranes (Anopore, Whatman International Ltd., Maidstone, England) can be used in place of the polycarbonate. The alumina pores provide higher aspect ratio, being $60 \mu\text{m}$ thick and having pore diameters of $0.2\text{--}0.02 \mu\text{m}$. Alumina filters can be etched by sodium hydroxide without causing damage to the polymer fibers. Figure 6c and d show PP fiber arrays created from polycarbonate and from alumina filters, respectively.

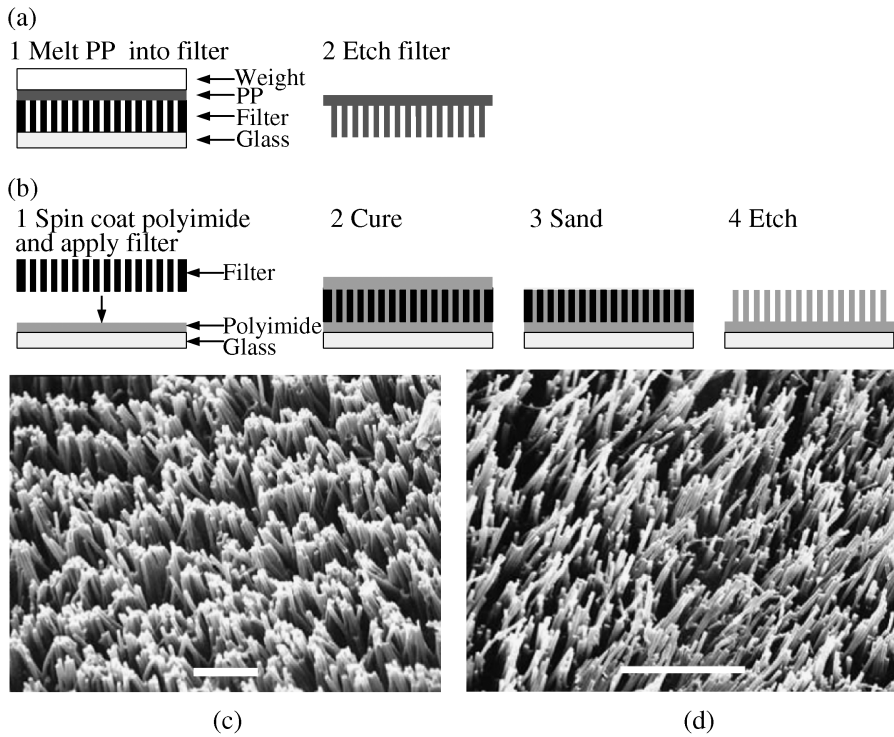


Figure 6. (a) PP casting and (b) PI casting in filters. (c) 0.8 μm diameter PP fibers created using a polycarbonate filter. (d) 0.2 μm diameter PP fibers created using an alumina filter. Scale bars are 10 μm .

It is also possible to create a reusable mold by templating a master fiber array. Figure 7a illustrates the process of curing poly(dimethylsiloxane) (PDMS) over a master. Then, once the PDMS has cured, the master is removed and the mold can be filled with polypropylene. After filling with polypropylene, the PDMS mold can simply be peeled off and reused.

Nickel (see Section 3.2) and polyimide fibers have both been used successfully as masters for templating at large diameters ($\geq 2.0 \mu\text{m}$). However, at smaller diameters, clumping and densely packed fibers prevent complete molding of the master. This results in a PDMS mold that has short, irregular pores. Examples of arrays created in PDMS molds are shown in Fig. 7. The larger diameter fibers in Fig. 7b turn out very uniform, whereas the smaller diameter fibers in Fig. 7c look short and mottled.

3.2. Electrodeposition

Electrodeposition in alumina or polycarbonate filters can produce nickel fiber arrays (Fig. 8a). As the figure shows, a filter is first attached to a conductive substrate such as metal shim, conductive epoxy, or silver colloidal paste. The nickel anode and filter are suspended in an electrolytic solution and voltage is supplied. Plating

After electroplating, but prior to etching, additional steps can be taken to produce unique tip structures. One possibility is to use the freshly over-plated filter as a cathode and continue plating. The newly exposed tips of the fibers will start to re-plate, so by controlling the time, spheres of various sizes can be achieved (Fig. 8b). Alternatively, if the filter is lightly polished with a sandpaper, the tips of the fibers will become angled (Fig. 8c). These structures are interesting because, along with the PDMS-templating mentioned above, it should be possible to make polymer copies.

4. DESIGN CHALLENGES

When casting fibers, the quality of the array depends on the quality of the mold. Because the filters have a random pattern of pores, a number of complications arise from their use. We have identified some of these problems and devised methods to lessen their effect.

4.1. Clumping

Clumping of fibers attenuates the adhesion of arrays by limiting a group of fibers' ability to conform to a surface. Clumping of cast fibers occurs at any size scale because of the random spacing of the pores used for molding. However, clumping is markedly more severe as the aspect ratio of the fibers increases.

Using elastic rod theory, the critical spacing, Δ_{cr} , between adjacent fibers necessary to avoid clumping controlled by tip-tip adhesion (see Fig. 9a) is shown in [27] to be

$$\Delta_{\text{cr-tip}} = \frac{2F_s L^3}{3EI} = \frac{2L^3 W_{\text{ad}}}{ER^3}, \quad (12)$$

where it is assumed that the tips are rounded and, following from the JKR theory [20] for a sphere contacting a sphere, have a bond strength of $F_s = 0.75\pi R W_{\text{ad}}$, where W_{ad} is the work of adhesion per unit area. If contact is allowed along the sides, as illustrated in Fig. 9b, then it follows from the principle of minimum potential energy that

$$\Delta_{\text{cr-side}} = \frac{L^2}{3} \sqrt{\frac{2\omega}{EI}}, \quad (13)$$

where ω is the energy of adhesion per unit area of contact between adjacent fibers [11]. For elastic cylinders,

$$\omega = 6 \left\{ \frac{(1 - \nu^2) R^2 W_{\text{ad}}^4}{\pi E} \right\}^{1/3}, \quad (14)$$

where ν is Poisson's ratio [12].

Equations (12) and (13) show that one strategy to avoid clumping is to simply vary design parameters such as length, radius and elastic modulus. However, this affects

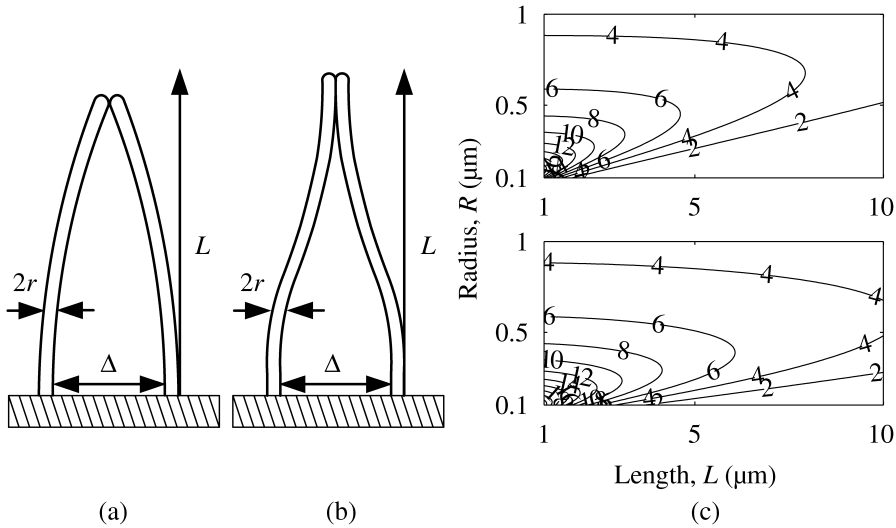


Figure 9. (a) Tip–tip clumping and (b) side-contact clumping model. (c) Plot of lines of constant adhesion pressure, P_{ad} , in N/cm^2 for a maximally packed array of fibers with prescribed length and radius; (top) tip–tip clumping model, (bottom) side-contact clumping model. These data were generated assuming polypropylene fibers, $E = 1 \text{ GPa}$, $W_{ad} = 30 \text{ mJ}/\text{m}^2$ and $\nu = 0.4$.

the density of fibers and/or the fiber compliance and thus reduces the strength of adhesion. These trade-offs can be evaluated by examining the pressure of adhesion, P_{ad} , that results from maximum packing and perfect contact of each individual fiber: $P_{ad} = F_o D_{cr}$, where $F_o = 1.5\pi R W_{ad}$ comes from the JKR theory for a sphere of radius R contacting a flat surface [20], and $D_{cr} = (\Delta_{cr} + 2R)^{-2}$. The values in Fig. 9c show that side clumping predicts a higher pressure. This results from the difficulty in maintaining a side clump, allowing the fibers to be placed closer together. Therefore, in a case where tip-clumping may be broken up during use, the fiber array may be designed according to the side-clumping constraints.

An alternative to tuning parameters is to prevent initial clumping due to fabrication. This can be accomplished with critical point drying (CPD) [28]. After filling of the mold is complete, the sample is etched in methylene chloride and transferred to isopropanol, which is removed by CPD. The use of CPD eliminates the formation of a meniscus between fibers which could draw them into contact. Fig. 10a shows a severely clumped array of fibers resulting from air drying while (b) shows the unclumped result of CPD.

While CPD limits clumping due to air drying, it cannot disengage already joined fibers. Therefore, fibers that are initially unclumped will start to adhere to one another as use of the array brings them into contact. A few data points can be acquired before the array becomes entangled. Figure 10c shows data from a CPD sample of $0.2 \mu\text{m}$ diameter, $30\text{--}60 \mu\text{m}$ long polyimide fibers using the two-axis force sensor (see Appendix A.2). The plot shows a pull-off force of almost 0.1 mN .

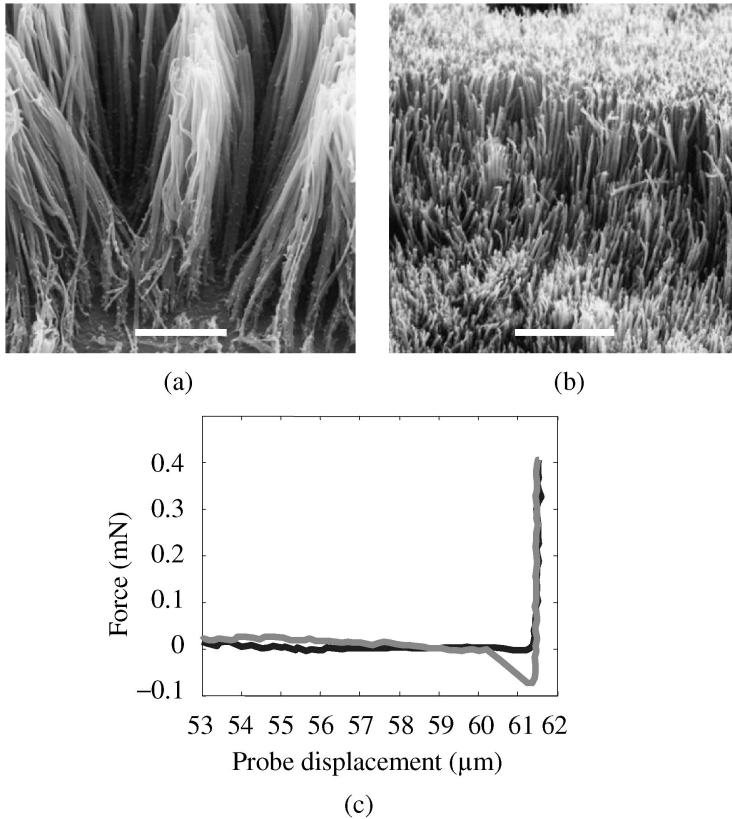


Figure 10. SEM images of $0.2\ \mu\text{m}$ diameter, $30\text{--}60\ \mu\text{m}$ long polyimide fibers (a) without critical point drying (CPD) and (b) with CPD (side views). Scale bars are $10\ \mu\text{m}$. (c) Shows pull-off measurements for polyimide fibers similar to (b).

Dividing this value by the contact area of the probe gives an approximate pull-off strength of $0.5\ \text{N}/\text{cm}^2$.

4.2. Backing curvature

Warping and curvature is another hurdle encountered when casting thermoplastic fiber arrays because of residual stresses in the substrate. The force needed to overcome these stresses is typically more than can be balanced by the adhesion force of the fibers. As a result, fibers, that might otherwise stick to the contacting surface, are pulled away by the backing after the preload is released. This is partly the reason why our previous hair patches that had a backing thickness of $\sim 50\ \mu\text{m}$ only showed remarkable friction [6], while our newer patches that have a backing $\sim 5\text{--}10\ \mu\text{m}$ thick are showing attachment in shear under zero load (see Fig. 1b).

This problem can be stated more concretely by considering the fracture of the adhesive bond between a naturally curved plate and a flat plate, as illustrated in Fig. 11. The curved plates have width b , length $2L$, thickness t and are assumed

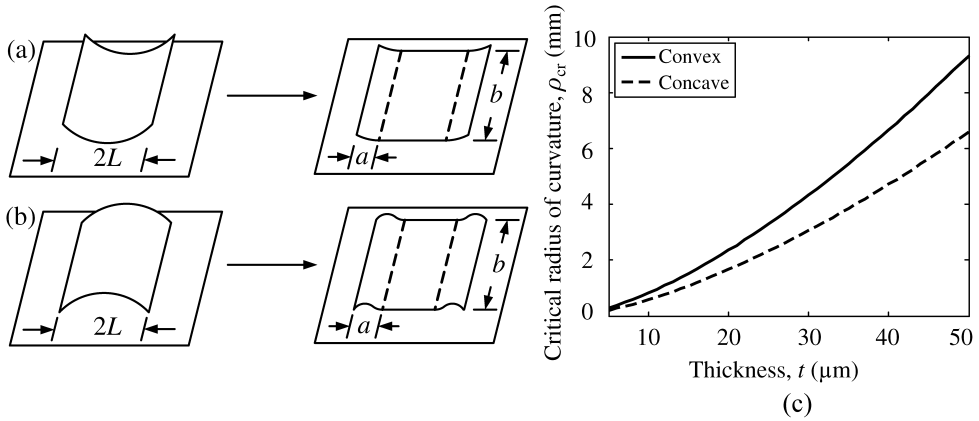


Figure 11. Flat plate in contact with (a) a convex plate or (b) a concave plate. (c) Plot showing the critical radius of curvature, ρ_{cr} , for a plate with $E = 1$ GPa and $W_{ad} = 30$ mJ/m². If the radius of curvature of a naturally curved plate is smaller than ρ_{cr} , then the plate cannot flatten by adhesion alone.

to behave linear elastically with modulus E . Also, initial cracks of length a are assumed to be present due to surface defects, poor initial contact, or some external perturbation following attachment.

Kendall determined the critical radius of curvature ρ_{cr} for a naturally convex plate to remain adhered to a flat surface by minimizing the total potential energy of the system $U_t = U_{el} + W_{ad}ab$, where U_{el} is the elastic strain energy [29]. Following from the stationary condition $\partial U_t / \partial a = 0$,

$$\rho_{cr, \text{convex}} = \sqrt{\frac{Et^3}{24W_{ad}}}. \quad (15)$$

In the case of a naturally concave plate, the critical value ρ_{cr} is slightly different since the delaminated portions are subject to clamped–pinned rather than clamped–free edge conditions, as shown in Fig. 11. The concave solution is found by modifying the U_{el} in U_t and solving $\partial U_t / \partial a = 0$ for ρ_{cr} .

$$\rho_{cr, \text{concave}} = \sqrt{\frac{Et^3}{48W_{ad}}}. \quad (16)$$

Hence, a concave plate can tolerate a somewhat lower radius of curvature.

It is apparent from (15) and (16) that for a stiff material, changing the thickness is an easy way to overcome the effects of substrate curvature. For example, consider an array of polypropylene fibers ($E = 1$ GPa) that shows low adhesion ($W_{ad} = 30$ mJ/m²). Figure 11c shows that by changing the backing thickness from 50 μm to 5 μm , a sample that could not adhere to the flat surface if its radius of curvature was less than 9 mm can now tolerate radii of curvature down to 0.5 mm.

This change in tolerance could potentially allow a sample to show macroscale adhesion instead of complete delamination.

5. CONCLUSION

Elastic rod theory and contact laws guide the design of adhesive and high friction microstructures. As with natural setal arrays, these structures are composed of stiff material with an elastic modulus $E > 1$ GPa. Unlike softer materials, such as rubber and low molecular weight polymers, stiff materials have the advantage of wear and creep resistance, and represent a wide range of polymers, metals and ceramics. However, stiff materials lack the inherent compliance of softer materials, and require additional levels of design complexity to lower their effective modulus.

For vertically-aligned, high aspect ratio nanofibers, compliance comes from buckling, and high bond strength comes from side contact as described in Section 2.3.1. However, such structures have the propensity to adhere to their neighbors, forming large clumps, according to the theoretical models presented in Section 4.1, which show dependence upon fiber geometry, elasticity, surface energy and spacing. Furthermore, relying on buckling necessitates large preloads [4].

Microfibers have less tendency to clump since their elastic restoring forces often exceed the surface forces necessary to adhere to neighbors. This property, however, implies that microfibers are unlikely to adhere to an opposing substrate through side contact, so the adhesive bond of the fiber is dependent upon the small contact allowed by a rounded tip. Nonetheless, microfiber arrays can exhibit high friction, with a friction coefficient several orders of magnitude greater than that of the smooth material under pressures ranging from 0 to ~ 10 kPa. This phenomenon is explained in Section 2.2.2 with a fiber buckling model that is experimentally validated for various fiber geometries and loading conditions. However, the experimental fit to the Hertz contact model (Section 2.2.1) shows that the needed compliance for tack is not present in these fiber arrays.

Further compliance could be added during fabrication. Fabrication methods include polymer casting and electrodeposition and utilize a porous filter as a mold. Such methods yield arrays of microfibers that are similar in size and elasticity to natural gecko setae. The main differences, however, are a lack of compliance and specialized tips. Angling of fibers, like those shown in Fig. 8c, can generate extra compliance as demonstrated for the gecko in Section 2.1.1. For microfiber arrays that rely on tip contact, the development of tip structures could be critical for increasing contact area. Figure 8b gives an example of spherical tips, but spatular tips, like those of the gecko, should also be explored.

The interaction of fibers with their backing, as discussed in Section 4.2, is a basic example of how hierarchical structures can affect the overall compliance. The fiber backing is analogous to lamellar structures found in the gecko. By modifying the thickness of the backing, samples that show high friction are also able to show shear adhesion (see Fig. 1).

Simple vertically aligned fibers show novel friction properties, but they provide only marginal pull-off adhesion properties. Future higher performance designs will require enhanced overall compliance through angled fibers and hierarchical structures, as well as greater intimate contact through spatula-like terminals.

Acknowledgements

This work was supported by NSF NIRT (No. EEC034730), NSF NSEC, DARPA and Emhart Corporation. R. E. Groff was supported by a DCI post-doctoral fellowship.

REFERENCES

1. K. Autumn, Y. A. Liang, T. Hsieh, W. Zesch, W. P. Chan, T. W. Kenny, R. Fearing and R. J. Full, *Nature* **405**, 681–685 (2000).
2. K. Autumn, M. Sitti, Y. A. Liang, A. M. Peattie, W. R. Hansen, S. Sponberg, T. W. Kenny, R. Fearing, J. N. Israelachvili and R. J. Full, *Proc. Natl. Acad. Sci. USA* **99**, 12252–12256 (2002).
3. M. T. Northen and K. L. Turner, *Sensors and Actuators A* **130–131**, 583–587 (2006).
4. Y. Zhao, T. Tong, L. Delzet, A. Kashani, M. Meyyappan and A. Majumdar, *J. Vac. Sci. Technol. B* **24**, 331–335 (2006).
5. S. Gorb, M. Varenberg, A. Peressadko and J. Tuma, *J. Royal Soc. Interface* **4**, 271–275 (2007).
6. C. Majidi, R. E. Groff, Y. Maeno, B. Schubert, S. Baek, B. Bush, R. Maboudian, N. Gravish, M. Wilkinson, K. Autumn and R. S. Fearing, *Phys. Rev. Lett.* **97**, 076103 (2006).
7. S. Kim and M. Sitti, *Appl. Phys. Lett.* **89**, 261911 (2006).
8. S. Kim, M. Spenko, S. Trujillo, B. Heyneman, V. Mattoli and M. R. Cutkosky, in: *IEEE Conference on Robotics and Automation*, Rome, Italy, pp. 1268–1273 (2007).
9. K. Autumn, N. Gravish, M. Wilkinson, D. Santos, M. Spenko and M. Cutkosky, in: *Proceedings of the 30th Annual Meeting of the Adhesion Society*, Tampa, FL, pp. 58–60 (2007).
10. N. J. Glassmaker, T. Himeno, C. Y. Hui and J. Kim, *J. Royal Soc. Interface* **1**, 23–33 (2004).
11. C. Majidi, R. E. Groff and R. S. Fearing, in: *Proceedings of ASME Int. Mechanical Engineering Congress and Exposition*, Anaheim, CA (2004).
12. C. Majidi, R. E. Groff and R. S. Fearing, *J. Appl. Phys.* **98**, 103521 (2005).
13. W. R. Hansen and K. Autumn, *Proc. Natl. Acad. Sci. USA* **102**, 385–389 (2005).
14. M. Varenberg, A. Peressadko, S. Gorb and E. Arzt, *Appl. Phys. Lett.* **89**, 121905 (2006).
15. A. K. Geim, S. V. Dubonos, I. V. Grigorieva, K. S. Novoselov, A. A. Zhukov and S. Y. Shapoval, *Nature Mater.* **2**, 461–463 (2003).
16. K. Autumn, C. Majidi, R. E. Groff, A. Dittmore and R. S. Fearing, *J. Expl. Biol.* **209**, 3558–3568 (2006).
17. M. F. Ashby, *Proc. Roy. Soc. A* **454**, 1301–1321 (1998).
18. R. E. Barker, *J. Appl. Phys.* **34**, 107–116 (1963).
19. B. Bhushan, *Introduction to Tribology*, p. 338. Wiley, New York (2002).
20. K. L. Johnson, K. Kendall and A. D. Roberts, *Proc. Royal Soc. Lond. A* **324**, 301–313 (1971).
21. A. V. Pocius, *Adhesion and Adhesives Technology: An Introduction*, 2nd edn, pp. 251–255. Carl Hanser Verlag, Munich (2002).
22. A. Jagota and S. J. Bennison, *Integr. Comp. Biol.* **42**, 1140–1145 (2002).
23. D. Maugis, *Contact, Adhesion and Rupture of Elastic Solids*, pp. 240–262. Springer, Berlin (2000).
24. C. Majidi, *Mech. Res. Commun.* **34**, 85–90 (2007).

25. T. Tong, Y. Zhao, L. Delzeit, C. Majidi, R. E. Groff, P. Reddy, A. Majumdar, A. Kashani and M. Meyyappan, in: *Proceedings of ASME Integrated Nanosystems: Design, Synthesis and Applications*, Berkeley, CA (2005).
26. M. F. Yu, T. Kowaleski and R. S. Ruoff, *Phys. Rev. Lett.* **86**, 87–90 (2001).
27. M. Sitti and R. S. Fearing, *J. Adhesion Sci. Technol.* **18**, 1055–1074 (2003).
28. G. T. Mulhern, D. S. Soane and R. T. Howe, in: *Proc. 7th Int. Conf. on Solid-State Sensors and Actuators — Transducers*, Yokohama, Japan, pp. 296–300 (1993).
29. K. Kendall, *J. Phys. D: Appl. Phys.* **4**, 1186–1195 (1971).
30. M. Varenberg, A. Peressadko, A. S. Gorb, E. Arzt and S. Mroczek, *Rev. Sci. Instrum.* **77**, 066105 (2006).

APPENDIX A: TESTING

A.1. Pulley

Static friction as well as pure shear measurements are performed on a pulley apparatus like that shown in Fig. A.1a. A string attached to the back of the fiber array is run over a pulley and attached to a cup that allows incremental loading. The sample is placed on an acetone-cleaned glass slide where it is loaded by a brass weight. Figure 4 shows high friction data taken with this setup.

A.2. Two-axis force sensor

A two-axis force sensor system, Fig. A.1b, was developed to simultaneously observe the shear and normal forces generated by a fiber array. The system uses a spherical glass probe, which was chosen to eliminate problems arising from misalignment between a flat probe and sample, a simple alternative to more elaborate self-aligning systems [30]. It also provides a convenient comparison to JKR theory. The probe is mounted on a two-axis mechanical spring constructed from four double-cantilevers as shown in Fig. A.1b. Double cantilevers were chosen because, unlike single cantilevers, they do not couple tip deflection with tip rotation. The particular arrangement of four double-cantilevers was chosen so that two optical probes (MTI-2100 fiber optic measurement system with MTI-2062E edge probes, MTI Instruments, Albany, NY, USA. Resolution — 44 nm at 1 kHz, Range — 190 μm) could each measure displacement along a single axis while mounted on mechanical ground. The sample is mounted on a nanopositioning stage (P-611 Nanocube, Physik Instrumente, Irvine, CA, USA. Resolution — 10 nm, Range — 100 μm). The resolution and range of the system (70 μN , 160 mN) are determined by the spring constant of the double cantilever force sensor (axis 1: 1600 N/m, axis 2: 1400 N/m) in combination with the range and resolution of optical sensor and nanopositioning stage. Figures 3b and 10c both show data that were taken using this apparatus.

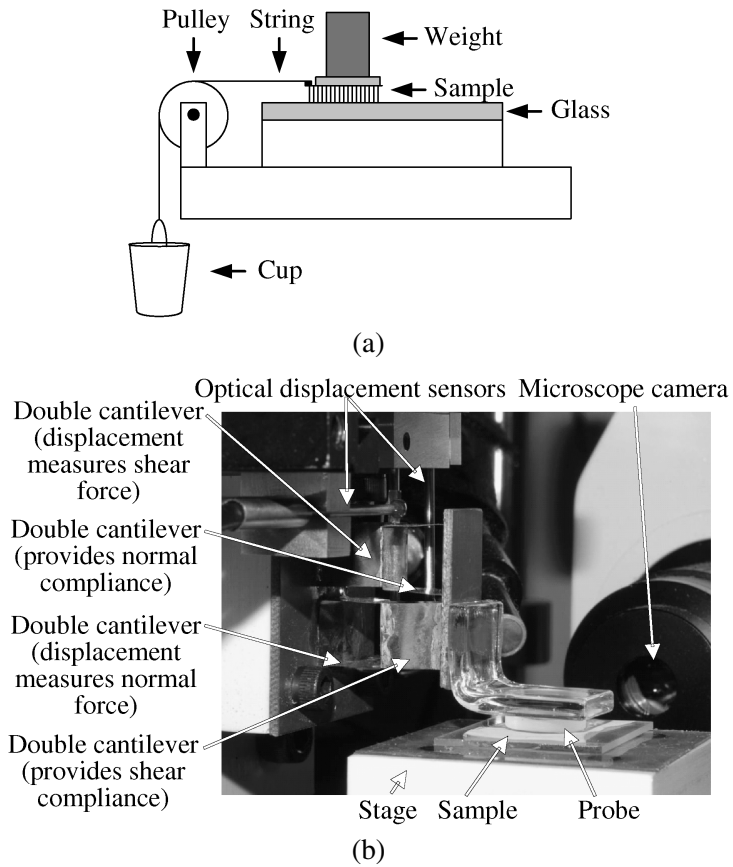


Figure A.1. Test equipment. (a) Pulley setup and (b) two-axis force sensor with spherical probe.